EUROPEAN ORGANIZATION FOR NUCLEAR RESEARCH
CERN - PS DIVISION

CTF3 Note 044 (MD)
PS/AE Note 2002-045
(Preliminary Phase)

CTF3 Preliminary Phase Commissioning Report on Fifth and Sixth Weeks, 3-14 December 2001

R. Corsini, B. Dupuy, L. Rinolfi, P. Royer (Ed.), F. Tecker
CERN, Geneva

A. Ferrari, Department of radiation sciences
Uppsala University

D. Alesini, C. Biscari, A. Drago, A. Ghigo, M. Masciarelli, M. Scampati, M. Serio
INFN - LNF, Frascati

Abstract

In this note, we describe the beam studies done during the fifth and sixth weeks of the commissioning of the Preliminary Phase of CTF3, from December 3^{rd} to December 14^{th} 2001. The beam was successfully injected into the ring and, after some injection optimisation, both the non-zero alpha and the isochronous optics were tested. In the non-zero alpha optics, about 4×10^{11} particles were accumulated in the ring, thus allowing tune and dispersion measurements. The extraction line was then successfully tested. Once the energy fluctuation issue was solved, a dispersion measurement was performed in the injection line, as well as a precise comparison between different energy measurement methods. Streak camera measurements in the linac and in the isochronous ring were also performed using both the CTF3 and the CTF2 streak cameras for comparison purpose.

Geneva, Switzerland
March 19, 2002

1 Goals

The main goal of this period was the commissioning of the ring. Both the non-zero alpha and the isochronous optics were tested and a large amount of time was dedicated to optimise the injection efficiency and the beam intensity in the ring in accumulation mode. Since the energy variation problem was solved during the first of the two weeks, we were also able to perform a new, precise dispersion measurement in the injection line, as well as a comparison of different energy measurement methods.

2 Start-Up

On the first day of operation, a magnet polarity check allowed us to detect that the connections between the quadrupole family HR.QTRB and the sextupole family HR.XNVB were inverted. This was rapidly corrected, as well as another connection error for two quadrupoles of the HR.QTRB family.

Last week of operation, we had noticed that WL.QNF351 was not well aligned and this had been corrected since. After this correction, the quadrupole WL.QNF352 also appeared to be misaligned. In addition, we observed a remanent magnetic field in the spectrometer magnet WL.BHZ36. All these effects had to be compensated using the available steering dipoles and the steering in the last part of the linac was indeed difficult and never perfect.

The timing of the RF signals were adjusted so that all pulses (up to five) have the same energy at the end of the linac. The settings in the pre-buncher and buncher were also modified for that purpose.

At the end of the first week, the problem of the energy variation was eventually identified: the 3 GHz RF source of the booster was not stable in frequency. The frequency generator was therefore replaced by a more stable 3 GHz synthesiser, and the fluctuations disappeared.

At some point, we noticed that the gun delivered an unstable current for the nominal bias value, as well as a varying pulse shape. This was mainly due to the declining Kentec amplifier, which was successfully replaced by some spare electronics during the second week of operation.

3 Energy measurements

The knowledge of the beam energy is essential for the commissioning of CTF3. Hence, we want to reduce the uncertainties on the energy measurement as much as possible. Several methods can be used to measure the energy at the end of the linac.

From the reading of the peak power meters, an analytical calculation of the energy gains in the accelerating structures of the linac can be performed with the following formula [1]:

$$\Delta E_k = \sum_{i=1}^{n} \sqrt{R_s \times L \times 10^{-\alpha_i/10} \times P_k} \tag{1}$$

where ΔE_k is the total energy gain for the n accelerating sections fed by the klystron k, R_s is the shunt impedance, L is the effective length of one accelerating section, α_i is the attenuation factor of the waveguides between the klystron k and the accelerating section i, and P_k is the peak power at the klystron output. In the following, we use $R_s = 54.2$ MΩ/m, $L = 4.572$ m and the following attenuation factors: $\alpha_{MDK25} = 6.41$, $\alpha_{MDK27} = 6.39$ and $\alpha_{MDK31} = 6.45$.

The beam energy can be measured directly with the spectrometer magnet WL.BHZ36 in the matching section. If the total deviation angle is $\Delta\theta$, the beam momentum is given by:

$$p\ [\text{GeV/c}] = \frac{\int B\text{d}l\ [\text{T.m}]}{3.3356\,\Delta\theta} \tag{2}$$

where the integrated field is a polynomial function of the input current in WL.BHZ36 as given in [2]. The same method can be applied using the dipole magnets HI.BSH00 and HIE.BHZ10 instead of WL.BHZ36. In that case, the calibration curve is given in [3].

Energy measurements have been performed with these three methods, for various values of the peak power in MDK31 and with $P(\text{MDK27}) = 34.6$ MW, see Figure 1. Several facts and/or assumptions can explain the discrepancies that we observed:

- in WL.BHZ36, a theoretical deviation angle of 35° was used in the calculation of the beam momentum. However, the calibration curve gives an angle of 36.67° for 332 MeV (measured in the injection line using HI.BSH00). Accurate position measurements on the SEM-Grid WL.MSH36 indicated that the actual value of this angle is 35.96°. A difference of 0.71° (12 mrad) remains to be explained. Nevertheless, the difference between the energies measured with WL.BHZ36 and with the magnets of the injection line is reduced (not represented on Figure 1).
- the good field region in WL.BHZ36 is also questionable and might slightly modify the deviation angle with respect to the expected value.
- the values of the attenuation factors between the klystrons and the accelerating structures are likely to be underestimated.
- the higher value of the energy when using the peak power meter reading might result from the fact that we measure the maximum available energy gain and that the mean value of energy is slightly lower than the maximum energy because of phase extension of the bunches on the RF curve.

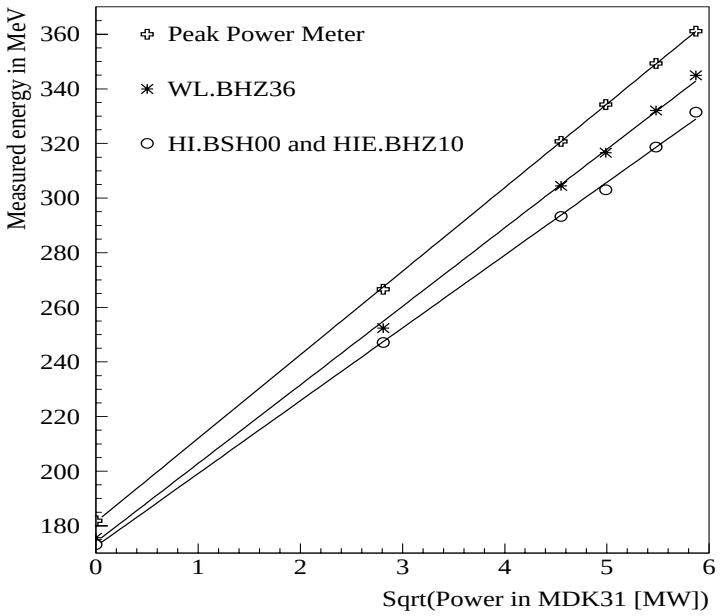

Figure 1: Measurement of the beam energy as a function of the peak power in MDK31, with three different methods (see text for details).

So far, it seems that the most accurate way to measure the energy is to use the injection line as a spectrometer. In the future, WL.BHZ36 needs to be calibrated again after taking into account its real deviation angle. We thus foresee to repeat this kind of measurements and also to use the circulating beam in the EPA ring to measure the energy.

4 Transverse beam dynamics in the linac

4.1 Quadrupole scans in the matching section

Two series of measurements were performed in the matching section, on December 6 and on December 12. Their purpose was to calculate the Twiss parameters at the exit of the last acceleration section, but also to check the stability of the machine. For both measurements, the beam energy was found to be 345.6 MeV in the SEM-Grid WL.MSH36, suggesting thus that the real beam energy be about 332 MeV (see Figure 1).

Each beam profile is fitted with a function $f(d) = cste + G_1(d) + G_2(d)$, where G_1 and G_2 are two Gaussian functions and d stands for the transverse direction x or y. After removing the constant term, the rms of the beam profile is calculated by only keeping the points for which the amplitude of the signal on the wire is larger than 10% of the maximum amplitude. With this method, we use a realistic fit function and we avoid taking into account the tails of the beam profile in the calculation of the rms bunch length. When performing the quadrupole scans in the matching section, the currents in WL.QNF352 and WL.QNF353 were set to 90.25 A and 30.31 A respectively, and the horizontal and vertical sizes of the beam in WL.WBS37 were measured as a function of the current in WL.QNF351. Although performed on different days, both scans are similar, which ensures the stability of the machine, as shown in Figure 2.

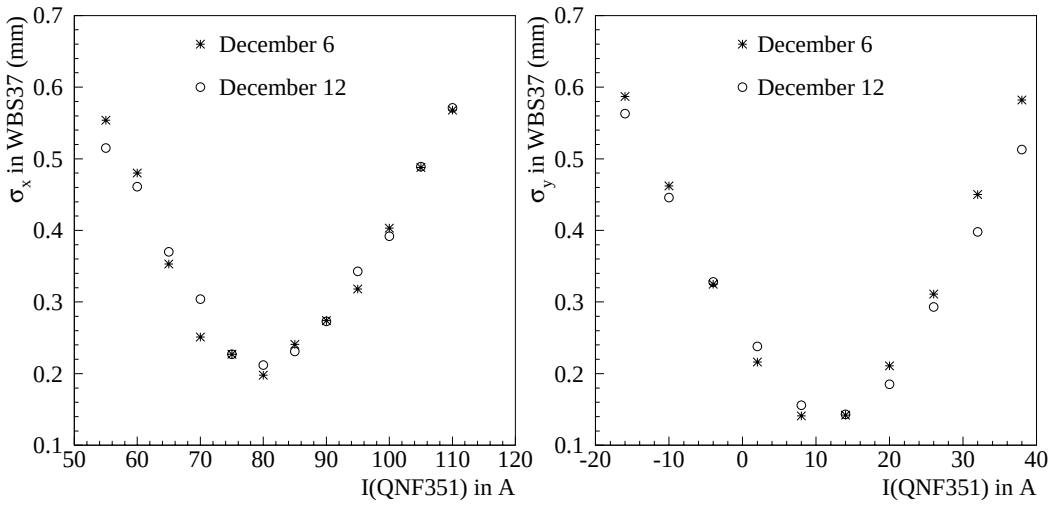

Figure 2: Transverse beam sizes in WL.WBS37 as a function of the current in WL.QNF351. Two series of measurements were performed.

The Twiss parameters and the normalised rms emittances at the entrance of WL.QNF351 that we derived from these quadrupole scans are given in Table 1. The emittances are much lower than the ones found during previous scans [3]. One possible explanation is that the present measurements were performed after the energy fluctuation issue was solved, contrary to the previous scans. Another possible explanation is that, when removing the tails from the transverse distributions, one reduces the rms beam size by a factor 1.2 or so, leading therefore to a reduction of the normalised emittance by about 1.5 compared to the case where all the points of the two-gaussian distribution are used for the calculation of the rms.

Twiss parameters	December 6	December 12
β_x (m)	21.49	18.41
α_x	-0.58	-0.45
ϵ_x (mm.mrad)	12	13
β_y (m)	45.04	31.80
α_y	-6.22	-4.22
ϵ_y (mm.mrad)	13	16

Table 1: Twiss parameters and normalised rms emittances calculated at the entrance of WL.QNF351 with a quadrupole scan in WL.WBS37.

4.2 Quadrupole scan in WL.WBS31

The lattice parameters at the entrance of WL.QLB29 were derived from the results of quadrupole scans in the matching section with a MAD simulation [4], see Table 2. On December 6, a second series of transverse measurements was performed, more upstream in the linac, in order to check the consistency of our results: the current in the quadrupoles of the WL.QNFB family was set to 27 A, and we measured the horizontal and vertical sizes of the beam in WL.WBS31 as a function of the current in WL.QLB29. The same scan was simulated with the initial Twiss parameters of Table 2. Figure 3 shows that there is a fair agreement between the experimental and simulated quadrupole scans, which confirms once again that the model used in order to simulate the linac optics and to predict the behaviour of the beam in the transverse planes is reliable.

Twiss parameters	December 6	December 12
β_x (m)	50.94	43.44
α_x	-8.28	-7.03
β_y (m)	29.27	27.79
α_y	-3.72	-3.14

Table 2: Twiss parameters at the entrance of WL.QLB29 derived from the results of the quadrupole scans in WL.WBS37.

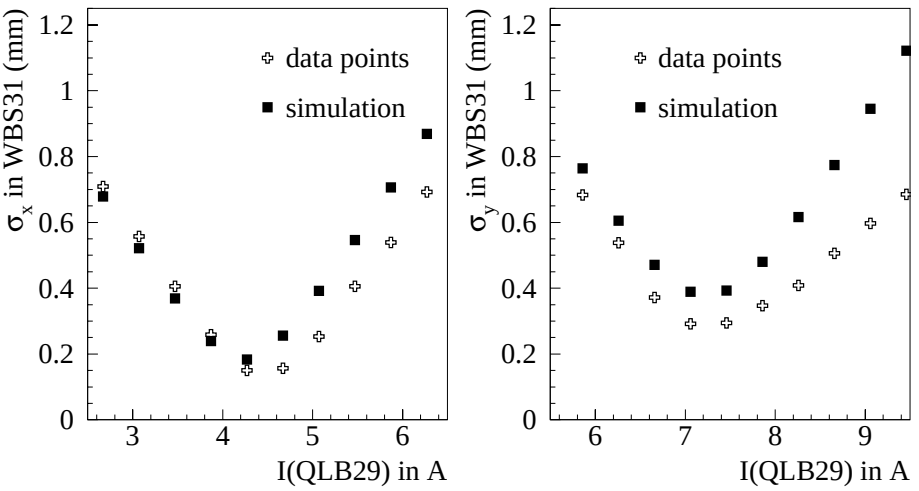

Figure 3: Transverse beam sizes in WL.WBS31 as a function of the current in WL.QLB29: the open crosses show the data points, while full squares show the simulated points.

5 Streak camera measurement in the linac

During the first week, streak camera measurements took place in the linac using the Cherenkov screen of WL.TCM37 with the new CCD camera mounted on the CTF3 streak camera. The current was set to its nominal value of 100×10^8 electrons in WL.UMA37 and a 550 nm filter was used in front of the camera. At the highest sweep speed, we measured the rms bunch length as a function of the slit width. The results giving the average rms bunch length calculated over a few pictures are summarised in Table 3 [5]. The real value of the bunch length is approached by reducing the slit aperture. The smallest value of 4.2 ps rms is indeed consistent with a rms bunch length of 3.3 ps (corresponding to 8 ps FWHM) when taking into account a resolution of 2.5 ps for the streak camera.

Slit Width	RMS Bunch Length [ps]
slit max	9.2
slit 2.8	6.8
slit 2.75	5.9
slit min	4.2

Table 3: Average rms bunch length as a function of the slit width.

Some tests were performed using the transition screen of WL.TCM37, but the light intensity was lower than with the Cherenkov screen. Some preliminary tests were also done using WL.TCM36 in the spectrometer line, but no relevant data were taken.

During the second week, the CTF2 streak camera was installed and a comparison of the measured bunch length between the Cherenkov screen and the Transition screen was carried out using WL.TCM37. The CTF2 streak camera allows to go down to a sweep speed of 10 ps/mm. We therefore studied the following sweep speeds: 50 ps/mm, 25 ps/mm and 10 ps/mm. Table 4 summarises the results that were obtained. The Cherenkov and Transition monitors measured roughly the same bunch length for the first two sweep speeds. At the sweep speed of 10 ps/mm, the light intensity was not sufficient to use the transition signal. By going to lower sweep speed, we increased the resolution of the measurement and observed that the apparent bunch length decreased.

Sweep Speed [ps/mm]	RMS Bunch Length Cherenkov [ps]	RMS Bunch Length Transition [ps]
50	7.7	7.8
25	6.1	6.0
10	5.4	-

Table 4: Comparison of the measured bunch length with the Cherenkov and Transition monitors using the CTF2 streak camera. Each value is averaged over several bunch profiles [5].

6 Dispersion measurement in the injection line

Precise dispersion measurements took place in the injection line, in order to check the consistency of the dispersion pattern between the experimental settings (see Section 7.1) and the nominal optics. For this measurement, we used all the diagnostics available in the injection line: the cameras HIE.MTV01, HIE.MTV23, HIE.MTV30, the pick-up HIE.UMA23 and the SEM-Grid HIE.MSH23. Starting from the experimentally optimised optics, we scaled the current in all magnetic elements and recorded the corresponding beam position in each diagnostic tool. For each current setting, the corresponding energy was computed using the value of the current in the first dipole HI.BSH00. The results for the horizontal plane are summarised in Table 5.

Energy [MeV]	HIE.MTV01 [mm]	HIE.UMA23 [mm]	HIE.MTV23 [mm]	HIE.MSH23 [mm]	HIE.MTV30 [mm]
324	4	25.5	30	20	-13
327	2	15.2	18	16	-7
330	1	7.5	12	10	-2.5
333	-1	-1	1.25	2	2
336	-2.5	-9.7	-12	-9	7
339	-4	-19.2	-25	-20	12
342	-5	-28.2	-30	-30	13

Table 5: Horizontal beam deviations in each diagnostic tool for various energies in the injection line (the column order corresponds to the beam path).

The measurement resolution is very different from one diagnostic tool to the other: the pick-up is the most sensitive one while the cameras are less precise. Figure 4 shows the measured beam displacement in the horizontal plane in HIE.UMA23 as a function of the momentum deviation. The dashed curve is the least square fit of the data whereas the slope of the solid line shows the expected dispersion value for a zero energy error. For the pick-up, the error bars are very small ($\pm$1.5 mm).

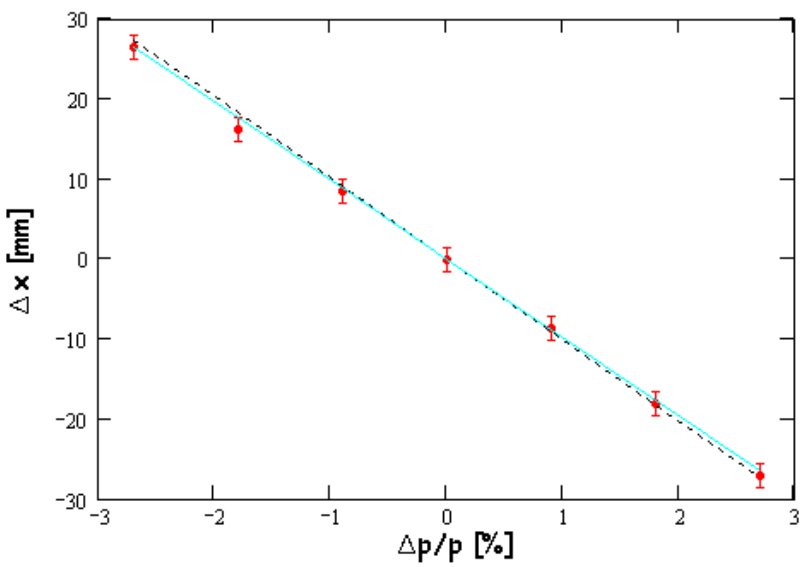

Figure 4: Horizontal deviation in HIE.UMA23 as a function of the momentum deviation.

Knowing the value of the current in each magnetic element, it is possible to compare the dispersion curve given by the MAD model with the measured values (see Figures 5 and 6). In the horizontal plane, there is a very good agreement between the measured and simulated values of the dispersion at each measurement point, and the full curve is very consistent with the points. In the vertical plane, the agreement between the measurement and the simulation is rather good, although the resolution becomes an issue since the expected values of the dispersion are very close to zero for most of the measurement points (in the cameras for instance). During the analysis, we noticed that the sign of the vertical displacement in HIE.UMA23 may be inverted since the model and the measurement give about the same value with an opposite sign (see Figure 6).

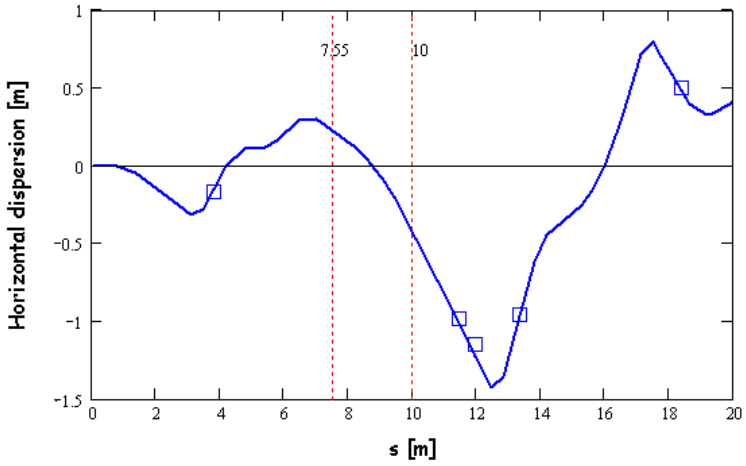

Figure 5: Horizontal dispersion measurement. The squares are the experimental points and the curve is given by the model for the corresponding current settings.

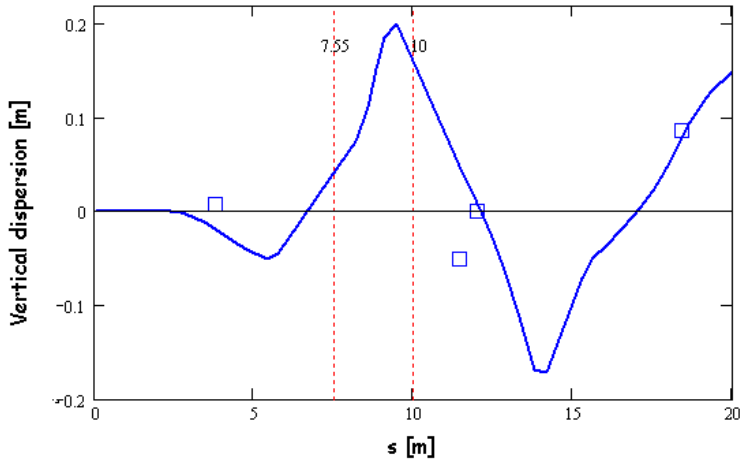

Figure 6: Vertical dispersion measurement. The squares are the experimental points and the curve is given by the model for the corresponding current settings.

Two additional UMAs will be installed at the locations indicated by the vertical dashed lines. These UMAs will provide two new measurement points to help characterise the dispersion behaviour along the transfer line with a greater precision.

7 Beam in the EPA ring

7.1 Injection in the ring

During the first week, the first attempts to inject the beam in the ring were successful. In order to achieve axial injection, we adjusted the timing and the amplitude of the injection kicker HR.KFI91 and the amplitude of the injection septum HIE.SMH33. In order to compensate for an imprecise matching at the entrance of the transfer line, we also modified the settings of the injection line compared to the nominal optics: the current in the quadrupoles HIE.QDW11, HIE.QFW25 and HIE.QFW30 was decreased by 21%, 27% and 11% respectively. In addition, the two following changes were experimentally found in the injection line:

- The currents in the vertical dipoles HIE.BVT00 and HIE.BVT30 were increased by 13% and 21% respectively (thus introducing an asymmetry compared to the model).
- The ratio of the currents in HI.BSH00 and HIE.BHZ10 was slightly modified compared to the theoretical one. It moved from $I_{BSH00}/I_{BHZ10} = 0.45$ to $I_{BSH00}/I_{BHZ10} = 0.44$ (this could be due to hysteresis in the magnets).

Using these settings, we managed to observe the first turns of the beam in the ring on the pick-up HR.UMA11, as shown on Figure 7. At this point, the RF cavity was not switched on and the beam was not accumulated yet.

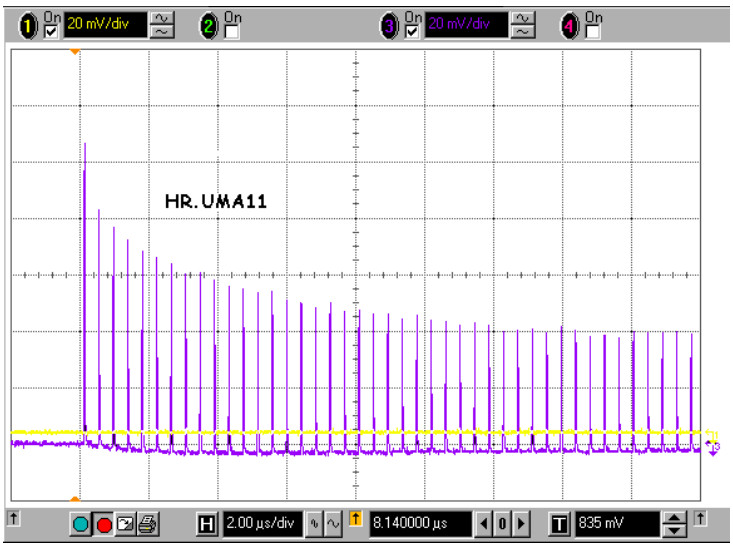

Figure 7: First turns of the beam in the EPA ring, observed on the pick-up HR.UMA11.

7.2 Accumulation

After a missing module was reinstalled in the RF electronics, the RF cavity was switched on, with the machine working in the accumulation mode. In order to move away from the axial injection, the settings of the kickers and the septa were slightly modified. The beam was first captured with an injection efficiency at the first turn close to 95% (as given by the ratio of the sum signals of HIE.UMA23 and HR.UMA91, see Figure 8), but the losses after the first turn were important and the overall capture efficiency was small. Another setting then allowed to capture more beam with a lower injection efficiency at the first turn. Eventually, after some optimisation, a total of 4×10^{11} particles were accumulated (see Figure 9), with one bucket filled (out of eight).

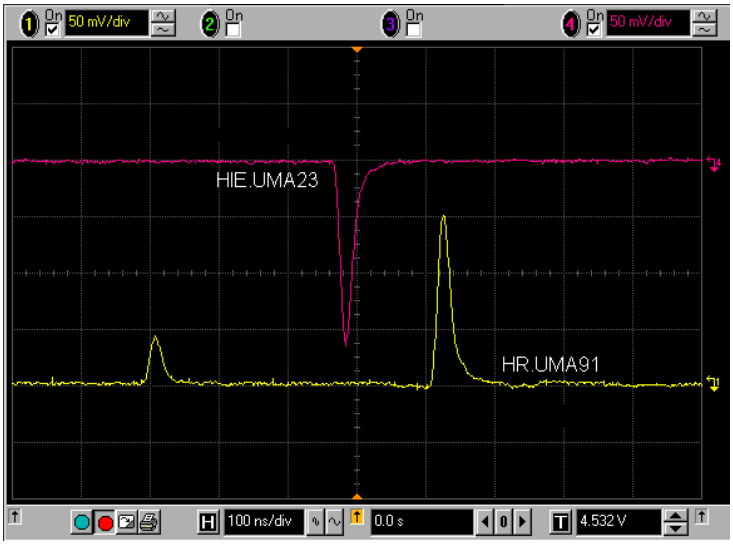

Figure 8: Beam position monitor signals in the injection line (HIE.UMA23) and in the ring (HR.UMA91). The injection efficiency is close to 95%. The small pick on the left is the accumulated beam.

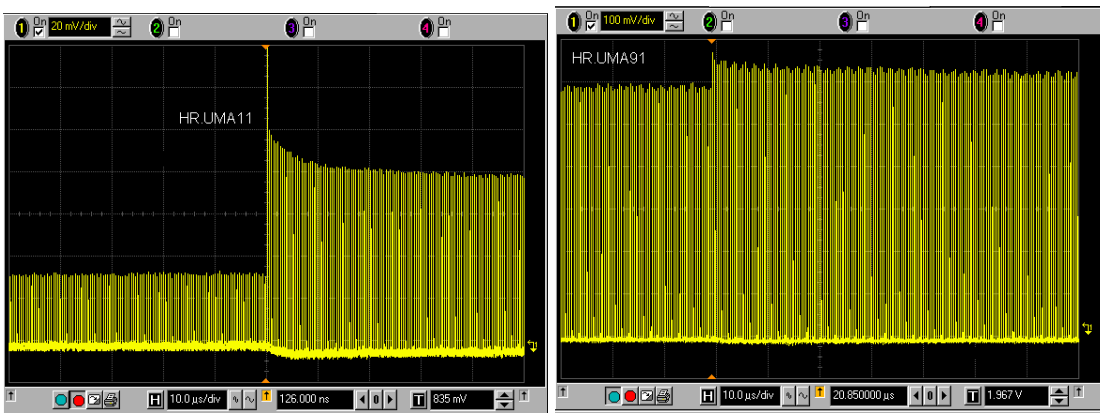

Figure 9: Accumulated beam in the EPA ring in accumulation mode. Left: First captured beam. Right: Maximum accumulated current, 150 mA (4×10^{11} particles).

Some new experimental current settings were found in the ring during the accumulation optimisation. The comparison between the nominal and the experimental currents is given in Table 6 for the operation at 332 MeV (computed from the current in the EPA bending magnets). The major modifications concern the two quadrupole families HR.QFLA and HR.QFWB, for which the currents were modified by 14% and 20% respectively compared to the nominal optics. These changes still have to be understood.

Magnet	I_{nom} [A]	I_{exp} [A]	I_{exp}/I_{nom}
HR.BHZ	288.00	288.04	$\sim$1
HR.QFWA	45.15	44.41	0.98
HR.QFWB	19.45	15.60	0.80
HR.QFLA	91.06	78.39	0.86
HR.QFLB	-44.84	-46.54	1.04
HR.QFI	18.95	18.78	$\sim$1
HR.QFN	22.00	23.26	1.06
HR.QDN	22.10	22.13	$\sim$1
HR.QTRA	-10.72	-11.22	1.05
HR.QTRB	40.55	41.59	1.03
HR.XNH	9.30	9.26	$\sim$1
HR.XNVA	27.22	29.61	1.09
HR.XNVB	55.40	55.23	$\sim$1

Table 6: Nominal and experimental currents in the ring for the accumulation optics at 332 MeV. The sign of the current refers to the conventions used in operation except for the HR.XNH family where a sign error was found between the model and the machine during the data analysis.

7.3 Isochronous optics

The nominal isochronous optics was also tested, and it was relatively easy to inject the beam and make it circulate. In this case, the nominal current settings were satisfactory, and no change was necessary. Figure 10 shows the signal in the beam position monitor HR.UMA91 during the isochronous optics tests. High losses occur at the first turns, probably due to bad matching.

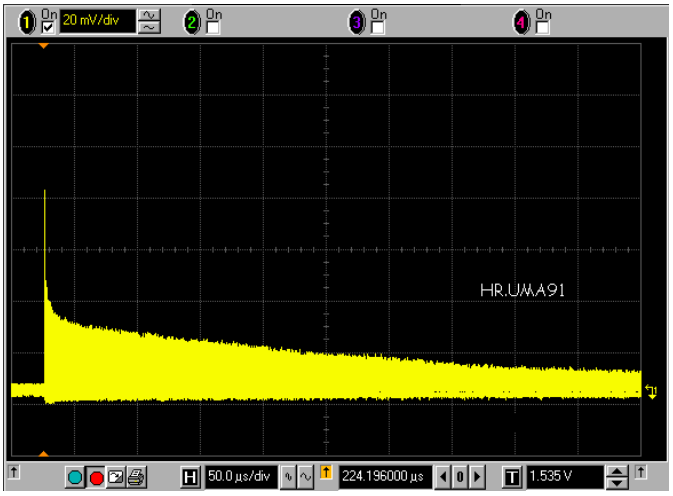

Figure 10: Circulating beam in the ring with the isochronous optics (more than 1000 turns).

7.4 Dispersion measurement in the EPA ring

The closed orbit of the EPA ring was measured for different RF frequencies. The frequency can be set by wheel switches on a box located in a rack next to the RF equipment in the HCR. An orbit measurement was taken for each RF setting. The magnet settings in the machine were the same as for the optimum accumulation optics (see Section 7.2).

Figure 11 shows an example of the closed orbit difference for two different frequency settings. The dispersion measurement shows the symmetry of the machine except for the outermost points, which might indicate a polarity inversion or other problem with HR.UMA03 or HR.UMA97.

The measured dispersion was then compared to the calculated dispersion from the MAD model using the measured quadrupole currents. The agreement is not very good (see dashed curve in Figure 11). Hence, the quadrupole currents in the MAD model were varied to match the measured dispersion pattern in order to find the most probable reason for the discrepancy.

When varying all currents, most currents were found to be close to the settings except for three quadrupole families. Matching individual families one at a time showed that the measured dispersion can be well reproduced with the current of HR.QFLA changed from 78.36 to 88.08 A. The corresponding dispersion curve is also shown in Figure 11. It matches the measured values very well and indicates that the above mentioned problem is a sign inversion on HR.UMA97.

Trying to match the dispersion with all families but HR.QFLA was not successful. This is a strong indication that there is a problem with either the current calibration of the power supply or the field calibration in the MAD model for HR.QFLA. Both possibilities will be investigated.

Using the dispersion D_x of the model at the UMA locations, the momentum deviation $\Delta p/p$ can be calculated from the orbit by

$$\left\langle \Delta p/p \right\rangle = \sum_{\mathrm{UMA}} \left(x \cdot D_x\right) \Big/ \sum_{\mathrm{UMA}} D_x^2 \quad . \tag{3}$$

This was done for the different orbits obtained with the MAD model, with an adjusted current in HR.QFLA. Figure 12 shows the calculated momentum deviation versus frequency change.

The closed orbit measurements were performed close to $f_0 = 19.085264\,\mathrm{MHz}$, the eighth harmonic of the former EPA revolution frequency, and the measurement points are therefore not centred around the real nominal frequency of $f_0 = 19.087955\,\mathrm{MHz}$. Extrapolating the curve to $\Delta f = 0$ shows a momentum error of $0.1\,\%$. The momentum compaction factor α was calculated from the fitted slope to be 0.06. This is consistent with the model calculation in this case which gives $\alpha = 0.056$.

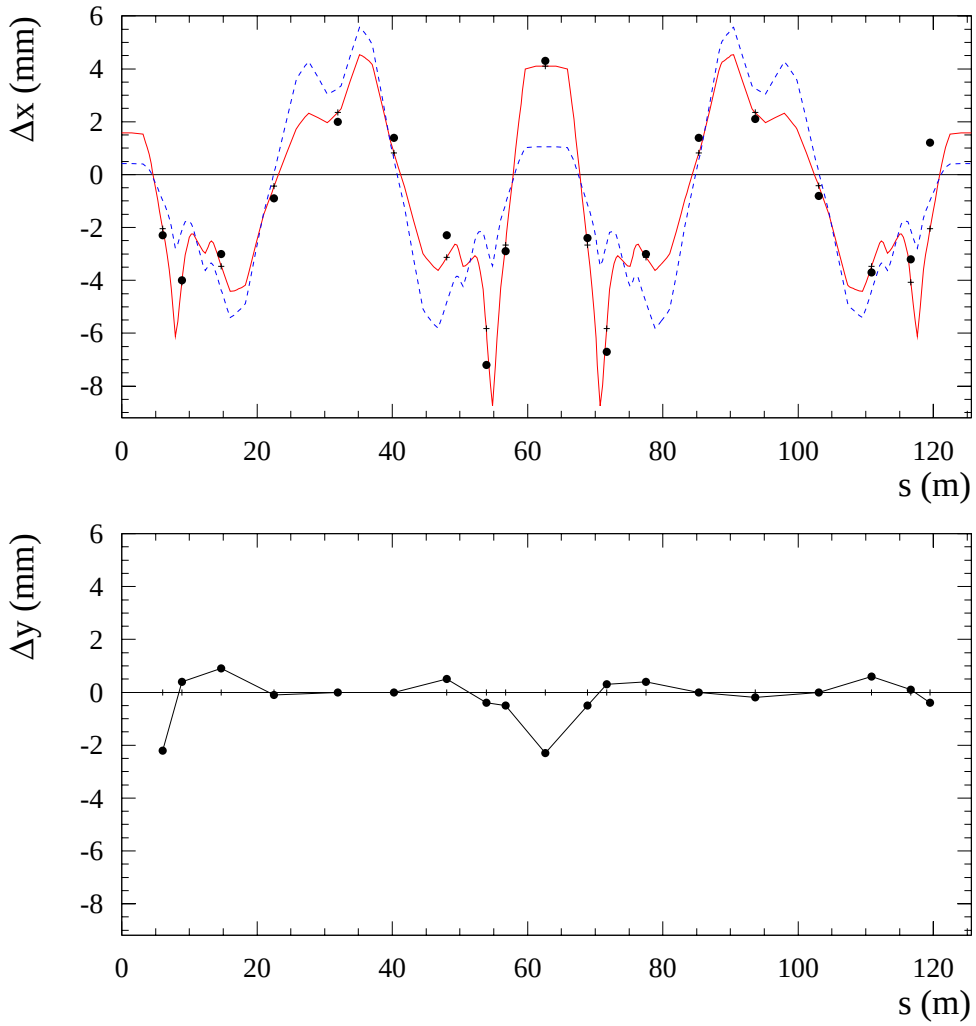

Figure 11: Measured closed orbit difference (black points) in the horizontal (top) and vertical (bottom) plane for a change in RF frequency from 19.084525 to 19.086814 MHz. The dashed line corresponds to the dispersion from a model with the measured currents. The solid line is the dispersion after changing the current in HR.QFLA in the model, the crosses mark the locations of the UMAs on this curve.

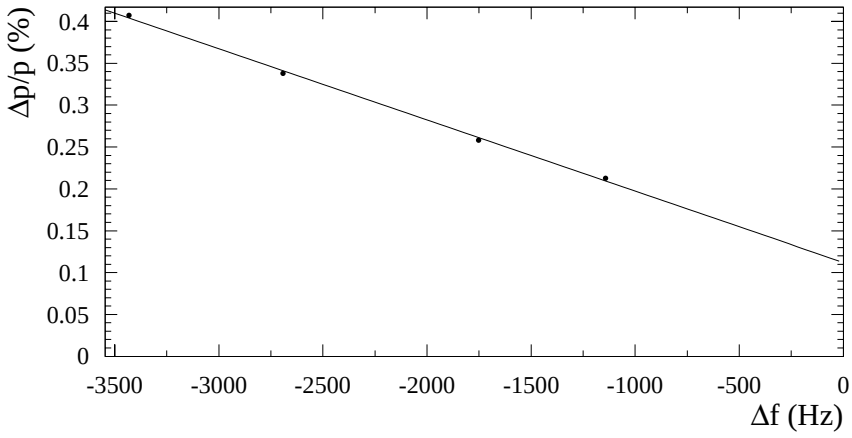

Figure 12: Calculated momentum deviation Δp/p versus frequency change Δf.

7.5 Tune measurement in the EPA ring

During the last day of operation, a few hours were dedicated to tune measurements in the ring. We started from the experimental configuration of the machine, where injection and accumulation were optimised. By varying the current in the HR.QTRB quadrupole family, we studied four different machine configurations and monitored the Fourier Transforms of the horizontal signal of the beam position monitor HR.UMA11. Figure 13 shows an example of the FFT signal and Table 7 summarises the results in both planes. The choice between q or $1-q$ is made according to the sign of the variation given by the MAD model for the same change in the current. For unknown reasons, the ring model fails to reproduce the values of the tune. Taking into account the alternative current of 88.08 A for the HR.QFLA quadrupole family (see Section 7.4) does not improve significantly the concordance, although the simulation results become closer to the experimental values in the horizontal plane. Various tracks are being investigated to understand this discrepancy between the model and the measurements.

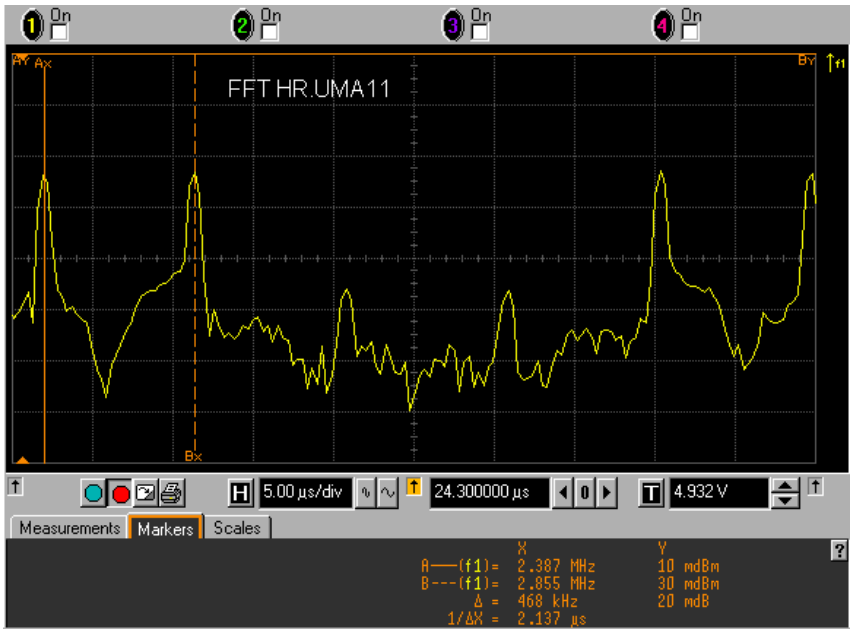

Figure 13: Example of the FFT signal on the horizontal signal in HR.UMA11. From left to right, the first peak corresponds to the revolution frequency, the second is the horizontal tune sideband, and two smaller ones are the vertical sidebands (resulting from coupling).

I_{QTRB} [A]	q_h	q_v
37.6	0.762	-
39.6	0.772	0.458
41.6	0.785	0.439
43.6	0.804	0.394

Table 7: Horizontal and vertical tunes as a function of the current in the quadrupole family HR.QTRB. The integer part of the tune is 4.

7.6 Streak camera measurement in the ring

During the second week, the CTF2 streak camera was installed in the synchrotron radiation laboratory, and was used to monitor the bunches in the ring, using the available synchrotron light ports MSR56 (dispersive region) and MSR58 (non-dispersive region).

The charge was approximately 30×10^8 in the ring and we put the nominal isochronous settings. We started using MSR58 where we easily found the beam in focus mode. However, the image seemed to correspond to an optical element (lens or mirror), and not to the beam itself. Moving to MSR56, the situation was better and we were able to have a focused image of the beam. Going to sweep mode at the sweep speed of 50 ps/mm, we recorded the bunch images after various numbers of turns in the ring, up to 20 turns. Figure 14 shows the evolution of the rms bunch length as a function of the number of turns in the ring [5]. Since the bunch length is almost constant, the optics was close to isochronicity, however the bunches are longer than expected even at the first turn (close to 20 ps rms). This could result from a non-isochronous transfer line or a bad matching at the injection. During data analysis, we noticed that the horizontal sextupole family had a wrong sign convention compared to the model, and a possible second order lengthening effect is investigated. Further data in the isochronous mode are needed in order to draw conclusions.

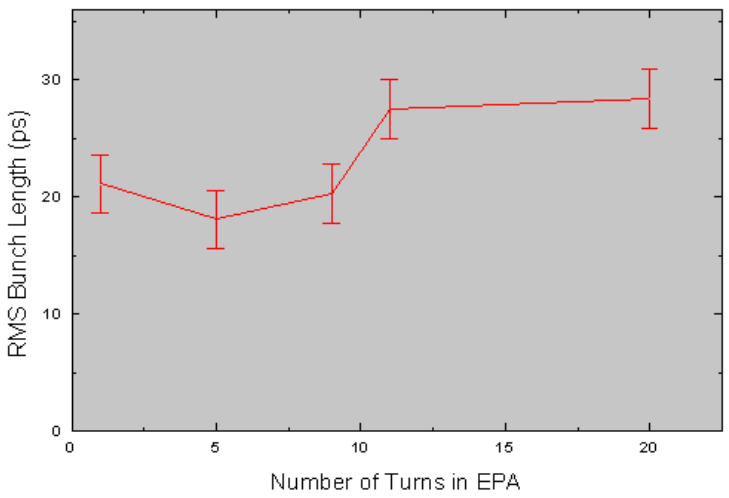

Figure 14: Evolution of the rms bunch length as a function of number of turns in the ring.

7.7 Beam extraction

An electron extraction line was made out of the former LPI positron injection line. The extraction process using the former positron injection kicker with a new timing was successfully tested during the last week of operation. After standard injection into the ring, we fired the extraction kicker HR.KFE11 and observed that the beam is extracted with an efficiency close to 100%. The beam signal was observed in the beam position monitor HEE.UMA04 located in the extraction line, as shown on Figure 15. In that case, the timing was set in order to extract the beam after 12 turns in the ring.

The setting for the coarse timing of the extraction kicker must follow the rule:

$$HX.SKFE11C = 29975 + 8 \times N$$

where N is the number of turns after which extraction should occur. The fine delay HX.SKFE11F was set to 66 ns during our tests. Using this tuning, we managed to extract the beam after 1, 10 and 100 turns.

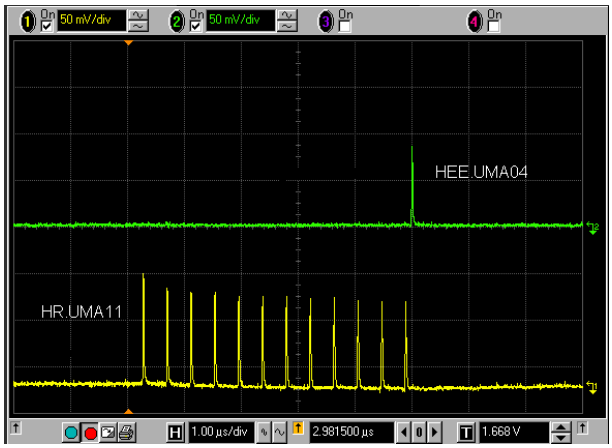

Figure 15: Circulating beam signal in the ring during 12 turns seen on HR.UMA11 (bottom signal) and extracted beam seen on HEE.UMA04 (top signal).

8 List of pending questions

The following issues will have to be addressed during the following commissioning sessions:

- Emittances have to be measured again in the linac without the energy fluctuations in order to explain the lower values on the last measurements.
- The correct matching at the entrance of the injection line must be implemented and the possible differences between the MAD model and the experimental optics of HIE have to be understood.
- The sign of the signals in HIE.UMA23 and HR.UMA97 have to be checked.
- The bunch length evolution has to be understood from the end of the linac (around 4 ps rms measured) up to the first turns in the ring in the isochronous optics (around 20 ps rms measured).
- More streak camera data are needed in both the linac and the ring to compare the bunch length value with the other methods.
- The independence of the bunch length with the number of turns in the isochronous optics has to be checked.
- The horizontal and vertical tunes have to be measured again in order to understand the discrepancy with the model.
- The fact that we had to increase the current of the HR.QFLA quadrupole family in the model in order to reproduce the dispersion measurement points must be investigated.
- In accumulation mode, the difference between the nominal and experimental optics of the ring must be clarified.

Acknowledgement
The research of A. Ferrari has been supported by a Marie Curie Fellowship of the European Community Programme ”Improving Human Research Potential and the Socio-economic Knowledge Base” under contract number HPMF-CT-2000-00865.

References

[1] R. Corsini, B. Dupuy, A. Ferrari, L. Rinolfi, T. Risselada, P. Royer and F. Tecker, “LIL lattice parameters, LIL energy gains, LIL temperature versus RF frequency, EPA circumference and EPA isochronicity measurements”, CTF3 Note 018, PS/AE Note 2001-011.
[2] R. Corsini, L. Rinolfi, T. Risselada, P. Royer (Ed.), F. Tecker, “CTF3 Preliminary Phase Commissioning - Report on Second Week, 8-12 October 2001”, CTF3 Note 037, PS/AE Note 2001-016.
[3] M. Belli, R. Corsini, B. Dupuy, A. Ferrari, C. Milardi, L. Rinolfi, P. Royer (Ed.), A. Stecchi and F. Tecker, “CTF3 Preliminary Phase Commissioning - Report on Third Week, 29 October - 2 November 2001”, CTF3 Note 040, PS/AE Note 2001-020.
[4] H. Grote and F. Ch. Iselin, “The MAD program”, CERN/SL/90-13(AP), Rev.3, 1993.
[5] T. Lefevre, Private communication.